

Acoustic topological phase transition induced by band inversion of high-order compound modes and robust pseudospin-dependent transport*

Yan Li(李妍)[†], Yi-Nuo Liu(刘一诺), and Xia Zhang(张霞)

School of Physics and Physical Engineering, Qufu Normal University, Qufu 273165, China

(Received 2 July 2020; revised manuscript received 30 July 2020; accepted manuscript online 7 August 2020)

A simple two-dimensional phononic crystal hosting topologically protected edge states is proposed to emulate the quantum spin Hall effect in electronic systems, whose phononic topological phase can be reconfigured through the rotation of scatters. In particular, the band inversion occurs between two pairs of high-order compound states, resulting in topological phase transition from trivial to nontrivial over a relatively broad high-frequency range. This is further evidenced by an effective Hamiltonian derived by the $k \cdot p$ perturbation theory. The phononic topology is related to a pseudo-time-reversal symmetry constructed by the point group symmetry of two doubly degenerate eigenstates. Numerical simulations unambiguously demonstrate robust helical edge states whose pseudospin indices are locked to the propagation direction along the interface between topologically trivial and nontrivial phononic crystals. Our designed phononic systems provide potential applications in robust acoustic signal transport along any desired path over a high-frequency range.

Keywords: topological phase transition, band inversion, compound mode, pseudospin

PACS: 63.20.-e, 43.35.Gk, 43.40.+s, 46.40.-f

DOI: 10.1088/1674-1056/abad21

1. Introduction

The discoveries of the quantum Hall effect (QHE)^[1] and the quantum spin Hall effect (QSHE)^[2] have boosted intense research of the topological phase transition and associated robust edge modes,^[3–5] which have strikingly revolutionized essential concepts of electric propagation in condensed matter systems. For the artificial crystals (e.g., photonic crystals and phononic crystals), both the crystal symmetry and the coupling strength among the scatterers can be altered flexibly. In consequence, the artificial crystals for classical waves offer an excellent platform to explore the quantum-like Hall effects and relevant topological physics. It has been revealed that the classical wave analogue of the topological insulators can be achieved in photonic systems,^[6–12] acoustic systems,^[13–28] and mechanical systems.^[29–37] Basically, the existing two-dimensional (2D) topological insulators for phononics can be classified into two categories: those mapping to integer quantum Hall effect (IQHE) with broken time-reversal (TR) symmetry,^[13–15,29,30] and those mimicking QSHE^[17–23,31–33] or quantum valley Hall effect (QVHE)^[24–28,35] with TR invariance. In the quest for constructing phononic topological states based on the IQHE, earlier pioneering approaches relied on circulating fluid flows,^[13,14] spinning gyroscopes,^[29,30] or active resonators^[15] to break the TR symmetry. However, the intrinsic noise and losses accompanying wave transmission in these nonreciprocal phononic systems, together with fabrication complexities, hinder their practical applications.

For another type of phononic topological insulators capitalizing on the physics of QSHE, the key mechanism is to construct the Kramers doublet, which is the prerequisite condition for the QSHE and guaranteed by the inherent half-integer spins in electric systems with TR invariance. The early attempts have been focused on elastic wave systems, in which different polarization modes, namely, the transverse polarizations and longitudinal polarizations, are combined together to emulate the spins of quantum systems.^[31,32] Recently, in the phononic crystals with double Dirac cones, two pairs of doubly degenerate Bloch modes have been utilized to construct pseudospin states and corresponding Kramers doublet, and the pseudospin-dependent unidirectional propagation with strong robustness has been demonstrated theoretically and experimentally in TR invariant systems.^[18–23] In addition to pseudospin, valley degree of freedom (DOF) has been demonstrated to be an extra controllable DOF for phononics.^[24–28,35] Two valleys with opposite valley-polarizations, which can be obtained by lifting the degeneracy of the Dirac cones at the Brillouin zone (BZ) corners, provide one efficient recipe to realize backscattering-immune valley transport.

In order to obtain pseudospin-dependent edge states in the phononic crystals with double Dirac cones, the vast majority of previous studies generally take advantage of the band inversion between the pseudospin dipoles and quadrupoles to generate the topological phase transition from trivial to nontrivial. By fine adjusting the filling ratio or material parameters of the

*Project supported by the Young Scientists Fund of the National Science Foundation of Shandong Province, China (Grant No. ZR2016AQ09) and Young Scientists Fund of the National Natural Science Foundation of China (Grant No. 11704219).

[†]Corresponding author. E-mail: liyanQFNU@163.com

scatterers, trivial and nontrivial bandgaps share a common but relatively narrow low-frequency range. In this paper, we design a 2D triangular phononic crystal consisting of anisotropic scatterers and propose a rotating-scatterer mechanism to realize band inversion between two pairs of doubly degenerate compound states in high-frequency range. More specifically, snowflake-like scatters are used to engineer a metamolecular crystal for intriguing band structures by simply rotating the scatters. In the rotational process, four-fold accidental degeneracy of higher-order compound modes appears at the BZ center, together with an acoustic quantum spin Hall phase transition. It is worth mentioning that the common bandgap of the topologically trivial and nontrivial phases is remarkably broad and possesses high frequencies. Based on the rotational symmetry of the primitive cell, we propose a pseudo-TR symmetry, which behaves in the same way as TR symmetry in electronic systems and renders the Kramers doublet in our designed phononic system. Furthermore, an effective Hamiltonian is developed to unveil the intrinsic link between the band inversion and the topological phase transition. Numerical simulations unambiguously demonstrate the backscattering-immune edge states that exist at the interface between two phononic crystals with different topological phases.

2. Triangular acoustic system

As depicted in Fig. 1, the snowflake-like metamolecule is constituted of one cylindrical rod and six three-legged rods. The 2D phononic crystal constructed by us possesses a triangular-lattice structure consisting of the snowflake-like metamolecules immersed in an air host. All the rods are made out of iron having mass density $\rho = 7670 \text{ kg/m}^3$, longitudinal wave velocity $c = 6010 \text{ m/s}$, and shear wave velocity $c_t = 3231 \text{ m/s}$. The background medium has mass density $\rho_0 = 1.21 \text{ kg/m}^3$ and speed of sound $c_0 = 343 \text{ m/s}$. We consider the following geometrical parameters: the width of the legs $h = 0.03a$, the length of the legs $d = 0.135a$, the radius of the cylindrical rods $r = 0.1a$, and the distance between the centers of cylindrical rods to the centers of three-legged rods $R = 0.27a$, with a being the lattice constant. Throughout this paper, the aforementioned geometrical parameters, i.e., the sizes of iron rods, are held constant. The orientation of the three-legged scatters is decided by the angle θ with respect to the horizontal axis. It is easy to see that if $\theta = 0^\circ$, the phononic system has a C_{6v} symmetry, including a six-fold rotational symmetry and six mirrors. By simply rotating the three-legged rods, the mirror symmetry of the primitive cell can be broken and a controllable bandgap with different topological phases can be achieved.

In our designed phononic crystals, due to the obvious distinction between the longitudinal wave velocity of iron and

that of air, the shear wave modes inside the iron components do not alter the fundamental physics of the system and can be ignored.^[38] By reasonably simplifying the wave modes, we consider the following acoustic wave equation in our periodic systems:

$$\nabla \cdot \left(\frac{1}{\rho_r(\mathbf{r})} \nabla p \right) = -\frac{\omega^2}{c_0^2} \frac{p}{B_r(\mathbf{r})}, \quad (1)$$

where p is the pressure, $\rho_r = \rho/\rho_0$ and $B_r = B/B_0$ denote the mass density and bulk modulus relative to those of the air, respectively, and $c_0 = \sqrt{B_0/\rho_0}$ represents the speed of sound in the air. Similar to the electronic crystals, the solutions of p in the periodic phononic systems can be written as Bloch wave functions $\Psi_{nk}(\mathbf{r}) = u_{nk}(\mathbf{r}) e^{i\mathbf{k}\cdot\mathbf{r}}$, with $u_{nk}(\mathbf{r})$ being a periodic function. The corresponding eigenfrequencies of these Bloch wave functions are ω_{nk} , whose dependence on the Bloch wave vector \mathbf{k} forms the n -th band of the dispersion relation. The orthogonality relation of these Bloch wave functions can be expressed as

$$\langle \Psi_{lk} | \frac{1}{B_r} | \Psi_{jk} \rangle = \frac{(2\pi)^2}{\Omega} \int \Psi_{lk}^*(\mathbf{r}) \frac{1}{B_r(\mathbf{r})} \Psi_{jk}(\mathbf{r}) d\mathbf{r} = \delta_{lj}, \quad (2)$$

where the integral is evaluated within a primitive cell with volume Ω , and δ_{lj} is the Kronecker delta. There are many approaches to solve the wave equation and obtain the dispersion relation, i.e., band structure. In this work, we use COMSOL Multiphysics (a commercial package based on the finite-element method) to calculate the band structure numerically.

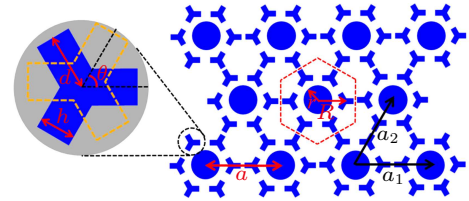


Fig. 1. Schematic view of a triangular phononic crystal consisting of snowflake-like metamolecules. Red dashed hexagon indicates the primitive cell composed by one cylindrical iron rod and six three-legged iron rods embedded in an air host. a is the lattice constant. a_1 and a_2 are the unit vectors. $R = 0.27a$ denotes the distance between the centers of cylindrical rods to the centers of three-legged rods. The radii of the center cylindrical rods are $r = 0.1a$. The width and length of the legs are $h = 0.03a$ and $d = 0.135a$, respectively. The angle θ with respect to the horizontal axis characterizes the orientation of the three-legged iron rods.

3. Band inversion and topological phase transition

To precisely explore the coupling physics between the center rod (marked as meta-atom A) and the six external rods (marked as meta-atom B) of the snowflake-like structure, we study the band structure and eigenstates for the proposed phononic crystal with the rotational angle $\theta = 23^\circ$, as shown in Fig. 2. It is observed that four doubly degenerate points (labeled as p^A , d^A , $p^A s^B$, and $d^A s^B$) emerge in the band structure at the Γ point. The corresponding eigenfields at the four points

are illustrated in Fig. 2(b), which reveal that the eigenmodes of such phononic system contain the center modes (superscript A) and the external modes (superscript B). As discussed in Ref. [39], the four pairs of doubly degenerate eigenmodes can be classified into two types: singleton modes (p^A and d^A) and compound modes (p^{A_sB} and d^{A_sB}). The eigenmodes p^A and d^A can be identified as dipolar and quadrupolar resonance states in meta-atom A, respectively. The eigenmodes p^{A_sB} combine dipolar states in meta-atom A with monopolar states in meta-atom B. And the eigenmodes d^{A_sB} correspond to quadrupolar states in meta-atom A and monopolar states in meta-atom B. It is worth noting that in meta-atom A, a pair of dipolar modes are accompanied by a pair of quadrupolar modes, and the dipoles possess opposite symmetry along the axes x and y of the primitive cell, whereas the quadrupoles obey identical symmetry along the axes x and y . Here we use $\sigma_{x,y} = +1, -1$ to represent even or odd symmetry along the axis x or y , respectively. For the two compound modes p^{A_sB} , one obeys symmetry $\sigma_x/\sigma_y = -1/+1$ and is named p_x mode, and the other obeys $\sigma_x/\sigma_y = +1/-1$ and is named p_y mode. For the two compound modes d^{A_sB} , one obeys symmetry $\sigma_x/\sigma_y = +1/+1$ and is named $d_{x^2-y^2}$ mode, and the other obeys $\sigma_x/\sigma_y = -1/-1$ and is named d_{xy} mode. By utilizing the eigenmodes p^A and d^A , topologically nontrivial bandgap has been achieved in many researches, but the bandgap is rela-

tively narrow and has low frequencies.^[18–20] In the following, we realize the band inversion between the higher-order compound modes p^{A_sB} and d^{A_sB} by rotating the three-legged rods. Specially, we obtain a wider bandgap with high frequencies.

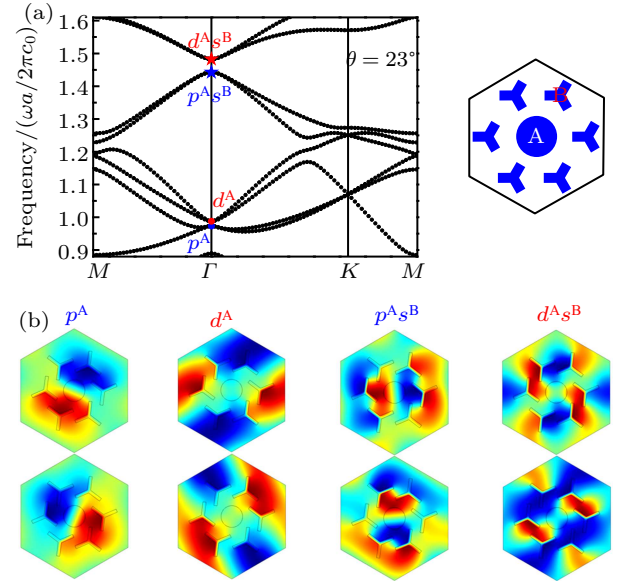


Fig. 2. (a) Band structure for the triangular phononic crystal with rotational angle $\theta = 23^\circ$. The right inset shows the primitive cell diagram. The cylindrical rod and three-legged rods are labeled as A and B, respectively. (b) Pressure field distributions of four pairs of doubly degenerate eigenstates, corresponding to the points p^A , d^A , p^{A_sB} , and d^{A_sB} from low frequency to high frequency in (a). Dark red and dark blue denote the positive and negative maxima, respectively.

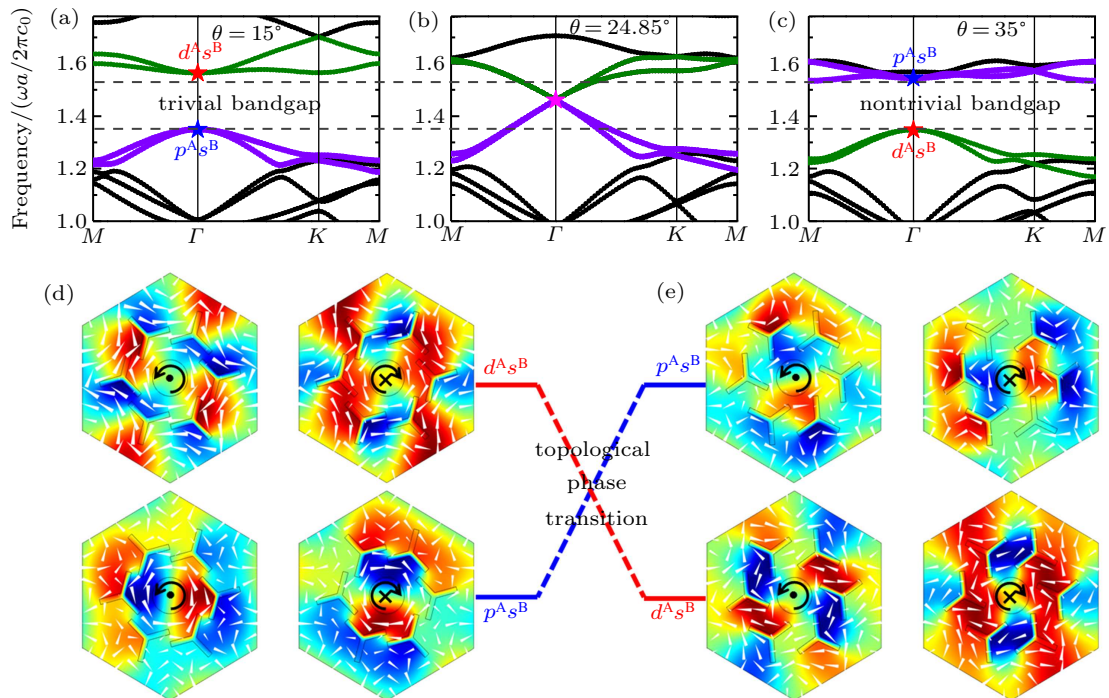


Fig. 3. (a)–(c) Band structures for the triangular phononic crystals with different rotational angles: (a) $\theta = 15^\circ$, (b) $\theta = 24.85^\circ$, and (c) $\theta = 35^\circ$. Green and violet dotted lines represent the bands including high-order compound modes p^{A_sB} and d^{A_sB} , respectively. (d), (e) Pressure field distributions of the modes p^{A_sB} and d^{A_sB} for phononic crystals shown in (a) and (c), respectively. The color patterns show the pressure distributions, where dark red and dark blue denote the positive and negative maxima, respectively. White arrows indicate the direction and amplitude of the time-averaged intensity. Black arrows show the spinning of sound intensity around the primitive cell center. The periodic boundary conditions are applied on the boundaries of the primitive cell.

As shown in Fig. 3(a), two double degeneracies, one for the lower bands including the modes $p^{A_s B}$ and the other for the upper bands containing the modes $d^{A_s B}$, appear at the BZ center for $\theta = 15^\circ$. Besides, with the increase of the rotational angle θ , the bandgap gradually decreases, the states $p^{A_s B}$ and $d^{A_s B}$ become degenerate at the Γ point for $\theta = 24.85^\circ$, and a double Dirac cone induced by four-fold accidental degeneracy is obtained as illustrated in Fig. 3(b). By further increasing the rotational angle θ , the four-fold degeneracy is destroyed and a phononic bandgap is reopened near the double Dirac point as shown in Fig. 3(c) for $\theta = 35^\circ$. The corresponding pressure field distributions of the doubly degenerate eigenmodes at the BZ center are exhibited in Fig. 3(e). It can be seen that the pressure fields at the lower-frequency side of the bandgap present $d^{A_s B}$ feature, those at the higher-frequency side of the bandgap display $p^{A_s B}$ feature. Namely, a band inversion is generated by rotating the three-legged rods, resulting in a topological phase transition from trivial to nontrivial. The trivial and nontrivial phononic crystals share a broad omnidirectional bandgap from the dimensionless frequency 1.3475 to 1.5341, just as demonstrated by the gray dashed lines in Figs. 3(a)–3(c).

4. Theory analysis of the topological property

According to the group theory, there are two 2D irreducible representations E_1 with basis functions (x, y) and E_2 with basis functions $(2xy, x^2 - y^2)$ at the Γ point of a triangular lattice. The representation E_1 has odd parity respective to spatial inversion operation, coinciding with the symmetry of doubly degenerate modes $p^{A_s B}$. However, the representation E_2 has even spatial parity, being consistent with the symmetry of doubly degenerate modes $d^{A_s B}$. Under the rotational operator with angle α , the matrix representation on basis (x, y) is

$$D_{E_1} = \begin{pmatrix} \cos \alpha & -\sin \alpha \\ \sin \alpha & \cos \alpha \end{pmatrix}. \quad (3)$$

By combining the matrix representation of $\pi/3$ rotation with that of $2\pi/3$ rotation, which are marked as $D_{E_1}(C_6)$ and $D_{E_1}(C_6^2)$, respectively, we define a unitary operator as follows:

$$U = \frac{1}{\sqrt{3}} [D_{E_1}(C_6) + D_{E_1}(C_6^2)] = -i\sigma_y, \quad (4)$$

where σ_y is the Pauli matrix. Together with complex conjugate operator K , we can construct an anti-unitary operator $T_s = UK$. It follows that

$$T_s^2 \begin{pmatrix} p_x \\ p_y \end{pmatrix} = T_s \begin{pmatrix} -p_y \\ p_x \end{pmatrix} = - \begin{pmatrix} p_x \\ p_y \end{pmatrix}, \quad (5)$$

which yields $T_s^2 = -I$. Similarly, by utilizing the E_2 matrix representations of rotational operators C_6 and C_6^2 on basis

$(2xy, x^2 - y^2)$, the unitary operator U can be defined as $U = [D_{E_2}(C_6) - D_{E_2}(C_6^2)]/\sqrt{3} = -i\sigma_y$. And the corresponding anti-unitary operator is constructed as $T_s = UK$, which also satisfies $T_s^2 = -I$. Obviously, for both E_1 and E_2 modes, the anti-unitary operator T_s behaves in the same way as the real TR symmetry in electronic systems and guarantees the appearance of the Kramers doublet in the current acoustic systems. Therefore, the T_s can be taken as a pseudo-TR operator. From the above derivations, it is easy to check that the crystal symmetry serves as a crucial role in composing the pseudo-TR symmetry.

Based on the angular momenta of the wave function of pressure fields $p^{A_s B}$ and $d^{A_s B}$, two pairs of pseudospin states are given by

$$p_{\pm} = \frac{p_x \pm ip_y}{\sqrt{2}}, \quad d_{\pm} = \frac{d_{x^2-y^2} \pm id_{xy}}{\sqrt{2}}, \quad (6)$$

where the subscripts “+” and “-” represent up and down pseudospins, respectively. To deliberately demonstrate the pseudospin characteristics, we examine the real-space distributions of the time-averaged intensity. Figures 3(c) and 3(e) show that the time-averaged intensity is circling around the primitive cell center, with the left-hand (right-hand) circular polarized chirality corresponding to the up (down) pseudospin.

On the basis (p_+, p_-) , the pseudo-TR operator is described as

$$T'_s = U'K, \quad (7)$$

where

$$U' = S^+US = \begin{pmatrix} -i & 0 \\ 0 & i \end{pmatrix}, \quad (8)$$

with S being the transformation matrix between the basis wave functions (p_+, p_-) and (p_x, p_y) . It is straightforward to see that

$$T'_s p_{\pm} = \mp i p_{\mp}; \quad T_s^2 p_{\pm} = -p_{\pm}. \quad (9)$$

Equation (9) clearly shows that the pseudo-TR operator transforms the pseudospin-up state into the pseudospin-down state, and vice versa. Hence the wave functions (p_+, p_-) are the two pseudospin states in the E_1 representation of our acoustic system. The same conclusion can be obtained on the wave functions (d_+, d_-) , which are the other pair of pseudospin states associated with the irreducible representation E_2 .

In order to further understand the topological property of the band inversion between the high-order compound pseudospin states, we construct an effective Hamiltonian in the vicinity of the BZ center based on the $k \cdot p$ perturbation theory.^[40,41] We denote the four eigenstates at the Γ point as Γ_{β} ($\beta = 1, 2, 3, 4$): $\Gamma_1 = p_x$, $\Gamma_2 = p_y$, $\Gamma_3 = d_{x^2-y^2}$, and $\Gamma_4 = d_{xy}$. The Bloch functions near the Γ point can be expanded as a linear combination of the four eigenfunctions Γ_{β}

$$\Psi_{nk}(\mathbf{r}) = \sum_{\beta} A_{n\beta}(\mathbf{k}) e^{i\mathbf{k} \cdot \mathbf{r}} \Gamma_{\beta}(\mathbf{r}). \quad (10)$$

Substituting Eq. (10) into Eq. (1) and utilizing the orthogonality relation of the four eigenfunctions Γ_β ($\beta = 1, 2, 3, 4$), we obtain the effective Hamiltonian around the Γ point

$$H_{mn}^{\text{eff}} = H'_{mn} + \sum_{\beta} \frac{H'_{m\beta} H'_{\beta n}}{\varepsilon_m^{(0)} - \varepsilon_\beta^{(0)}}, \quad (m, n = 1, 2, 3, 4), \quad (11)$$

where $\varepsilon_{1,2}^{(0)} = \varepsilon_p^0$ ($\varepsilon_{3,4}^{(0)} = \varepsilon_d^0$) is the eigenfrequency of $\Gamma_{1,2}$ ($\Gamma_{3,4}$), and $H' = \frac{2i}{\rho_r} k \cdot \nabla + ik \cdot \nabla \frac{1}{\rho_r} - \frac{k^2}{\rho_r}$ is the $k \cdot p$ perturbation term. On the basis (p_+, d_+, p_-, d_-) , the effective Hamiltonian around the Γ point can be rewritten as

$$H^{\text{eff}}(\mathbf{k}) = \begin{pmatrix} G - Dk^2 & Ck_+ & 0 & 0 \\ C^*k_- & -G + Dk^2 & 0 & 0 \\ 0 & 0 & G - Dk^2 & Ck_- \\ 0 & 0 & C^*k_+ & -G + Dk^2 \end{pmatrix}, \quad (12)$$

where $k_\pm = k_x \pm ik_y$, and $G = (\varepsilon_d^0 - \varepsilon_p^0)/2$ is the frequency difference between the E_2 and E_1 modes. Obviously, G is positive for the case shown in Fig. 3(a), but negative for the case shown in Fig. 3(c). C is calculated from the off-diagonal elements of the first-order perturbation term $H'_{mn} = \langle \Gamma_m | H' | \Gamma_n \rangle$ with $m = 1, 2$ and $n = 3, 4$. D is determined by the diagonal elements of the second-order perturbation term $H'_{m\beta} H'_{\beta n}$, and is typically negative. Based on Eq. (12), the spin Chern numbers^[11,18,21] can be evaluated as

$$C_\pm = \pm \frac{1}{2} [\text{sgn}(G) + \text{sgn}(D)]. \quad (13)$$

Due to $G > 0$ and $D < 0$ in the phononic system shown in Fig. 3(a), the spin Chern number $C_\pm = 0$, indicating that the bandgap is topologically trivial. On the contrary, for the phononic system shown in Fig. 3(c), $G < 0$ and $D < 0$, we obtain the spin Chern number $C_\pm = \pm 1$, which reveals that the bandgap is topologically nontrivial. In brief, we have validated a topological phase transition from a trivial state to a nontrivial state via band inversion, which is induced by simply rotating the three-legged rods.

5. Topologically protected edge states

Since the topologies for the phononic crystals shown in Figs. 3(a) and 3(c) are different, there will be unidirectional acoustic edge states at the interface separating these two systems. To validate the existence of these topologically protected edge states, we numerically calculate the projected band structure for a ribbon-shaped supercell, which comprises topologically nontrivial crystal after band inversion and topologically trivial crystal before band inversion, as shown in Fig. 4(a). By applying the periodic boundary condition on the x and y directions, we obtain the projected band structure as displayed in Fig. 4(b). It is found that in addition to the bulk states denoted by black dotted lines, there are doubly degenerate states spanning the bulk bandgap region, which are represented by red

dotted lines. After checking the pressure field distributions for the eigenstates at points E and F in Fig. 4(b), we discover that the pressure fields tightly localize at the interface and decay exponentially into bulk crystals on both sides. This means that the red dotted lines represent the dispersion relations of the edge states. Figures 4(c) and 4(d) present the real-space distributions of the pressure and time-averaged intensity fields on the upper interface at typical momenta with $k_x = \pm 0.1 \times \frac{4\pi}{3a}$, corresponding to points E and F in Fig. 4(b). It is clear that the intensity fields indicated by red arrows rotate clockwise and counterclockwise for the two opposite momenta, respectively. The chirality of sound intensity around the interface unveils the characteristics of the pseudospin-down and pseudospin-up states, coinciding with the feature manifested by Fig. 3. Here, we illustrate that the upper interface supports a TR pair of edge states with opposite propagation directions, i.e., a forward edge mode with down pseudospin and a backward edge mode with up pseudospin. However, the behavior of edge states is entirely reversed along the lower interface. Apparently, the locking of the pseudospin-up and pseudospin-down states with counter-propagations of edge modes is analogous to the property of QSHE in electronic systems.

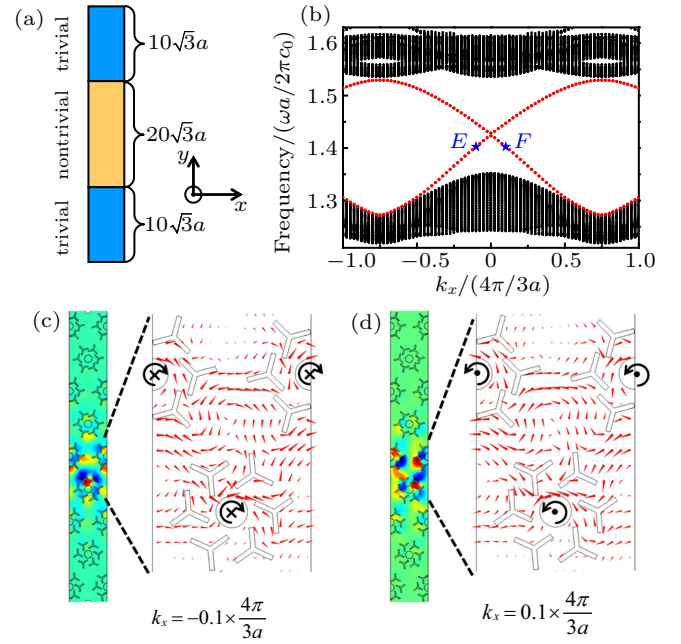


Fig. 4. (a) Schematic view of a ribbon-shaped supercell composed of the topologically nontrivial crystal ($\theta = 35^\circ$) with its two edges clad by topologically trivial crystal ($\theta = 15^\circ$). (b) Projected band structure for the ribbon-shaped supercell along the ΓK direction. The black and red dotted lines denote bulk and edge states, respectively. (c), (d) Pressure field distributions confined around the interface between two domains of distinct topology at points E and F indicated in (b), respectively. The corresponding intensity is displayed in the magnified views. The color patterns show the pressure distributions, where dark red and dark blue denote the positive and negative maxima, respectively. Red arrows show the direction and amplitude of the time-averaged intensity. Black arrows show the spinning of sound intensity around the primitive cell center. The periodic boundary conditions are applied on the x and y directions of the ribbon-shaped supercell.

As discussed in the previous section, it is possible for us to take advantage of the pseudospin Hall effect to realize acoustic helical edge states, i.e., utilizing the pseudospin DOF to control the propagation direction. The pseudospin specified edge states can be selectively excited by a point-like chiral source, which is an eight-antenna array with a $\pi/4$ phase delay between the neighboring ones as shown in Fig. 5(a). When the phases of these antennas gradually decrease clockwise (anticlockwise), the pseudospin-down (pseudospin-up) mode can be stimulated. Figures 5(b) and 5(c) display the pressure field distributions excited by the point-like chiral sources with clockwise and anticlockwise phase delays, respectively, in the air. In order to demonstrate the unidirectional propagation and robustness against perturbations of the pseudospin-dependent edge states, we combine the topologically trivial crystal with nontrivial crystal to construct a Z-shaped interface. As shown in Figs. 5(d) and 5(e), a point-like source with operating frequency $f \approx 1.4027c_0/a$, which corresponds to the frequency of the E and F points in Fig. 4(b), is placed at the location indicated by white circle. We observe that when the source has a clockwise phase delay, the acoustic wave propagates along the Z-shaped interface towards the upper left direction, manifesting the pseudospin-down edge state. On the contrary, the acoustic wave excited by the point-like source with anticlockwise phase delay propagates along the Z-shaped interface towards the lower right direction, revealing the pseudospin-up edge state. Besides, the simulated results also make clear that even though sharp bends are introduced at the interface, these pseudospin-dependent edge states robustly propagate along the Z-shaped interface without backscattering. It is evident that based on the pseudospin Hall effect induced by band inversion, we can manipulate acoustic waves to propagate along a selected path and direction without resorting to breaking the TRS.

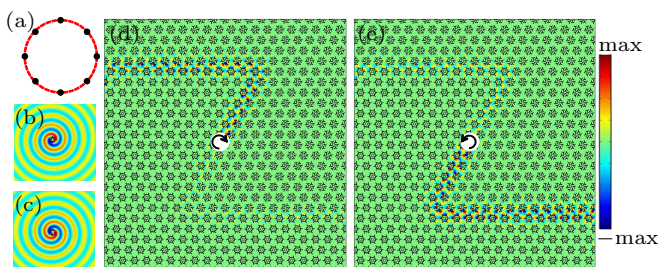


Fig. 5. (a) Schematic view of a point-like chiral source consisting of eight antennas, which has a phase difference of $\pi/4$ between the neighboring antennas. (b), (c) Pressure field distributions excited by the point-like chiral sources with clockwise and anticlockwise phase delays, respectively, in the air. (d), (e) Robustly unidirectional propagation of edge states along the Z-shaped interface between the topologically nontrivial and trivial crystals. The excitations in (d) and (e) correspond to the sources shown in (b) and (c), respectively. The white circle indicates the position of the point-like chiral source with operating frequency $f \approx 1.4027c_0/a$, whose phase delay direction is represented by the black arrow. The whole structure is surrounded by the perfectly matched layers to absorb outgoing waves.

6. Conclusion

We have designed a 2D acoustic topological insulator analogous to the QSHE in electronic systems. The topological insulator is a triangular phononic crystal consisting of snowflake-like metamolecules embedded in an air host. By rotating the three-legged rods within the primitive cell, band inversion is achieved between two pairs of high-order compound modes (i.e., doubly degenerate modes $p^A s^B$ and $d^A s^B$), and a noticeable topological bulk bandgap is obtained in the high-frequency range. Based on the point group symmetry of $p^A s^B$ and $d^A s^B$ eigenstates at the Γ point, we construct a pseudo-TR symmetry, which renders the Kramers doublet of acoustic pseudospins. By utilizing $k \cdot p$ perturbation theory, we propose an effective Hamiltonian around the Γ point, which unveils that the band inversion induces a topological phase transition from trivial to nontrivial. Numerical simulations explicitly manifest the unidirectional propagation and backscattering-immune property of the pseudospin-dependent edge states. The topological phononic crystal designed by us can be fabricated relatively easily, and its topological phase can be reconfigured just by simply changing the orientation of the three-legged rods. This is extremely advantageous for the potential applications in controlling acoustic waves along any desired path without backscattering. And the mechanism of band inversion between high-order compound states can be directly extended to electromagnetic wave systems.

References

- [1] Klitzing K v, Dorda G and Pepper M 1980 *Phys. Rev. Lett.* **45** 494
- [2] Kane C L and Mele E J 2005 *Phys. Rev. Lett.* **95** 226801
- [3] Bernevig B A, Hughes T L and Zhang S C 2006 *Science* **314** 1757
- [4] Hasan M Z and Kane C L 2010 *Rev. Mod. Phys.* **82** 3045
- [5] Qi X L and Zhang S C 2011 *Rev. Mod. Phys.* **83** 1057
- [6] Haldane F D and Raghu S 2008 *Phys. Rev. Lett.* **100** 013904
- [7] Wang Z, Chong Y D, Joannopoulos J D and Soljačić M 2008 *Phys. Rev. Lett.* **100** 013905
- [8] Liu K X, Shen L F and He S L 2012 *Opt. Lett.* **37** 4110
- [9] Chen W J, Jiang S J, Chen X D, Zhu B, Zhou L, Dong J W and Chan C T 2014 *Nat. Commun.* **5** 5782
- [10] Chen Y, Lin Z K, Chen H Y and Jiang J H 2020 *Phys. Rev. B* **101** 041109
- [11] Wu L H and Hu X 2015 *Phys. Rev. Lett.* **114** 223901
- [12] Yang Y T, Xu Y F, Xu T, Wang H X, Jiang J H, Hu X and Hang Z H 2018 *Phys. Rev. Lett.* **120** 217401
- [13] Khanikaev A B, Fleury R, Mousavi S H and Alù A 2015 *Nat. Commun.* **6** 8260
- [14] Yang Z J, Gao F, Shi X H, Lin X, Gao Z, Chong Y D and Zhang B L 2015 *Phys. Rev. Lett.* **114** 114301
- [15] Ding Y J, Peng Y G, Zhu Y F, Fan X D, Yang J, Liang B, Zhu X F, Wan X G and Cheng J C 2019 *Phys. Rev. Lett.* **122** 014302
- [16] Peng Y G, Qin C Z, Zhao D G, Shen Y X, Xu X Y, Bao M, Jia H and Zhu X F 2016 *Nat. Commun.* **7** 13368
- [17] He C, Li Z, Ni X, Sun X C, Yu S Y, Lu M H, Liu X P and Chen Y F 2016 *Appl. Phys. Lett.* **108** 031904
- [18] Mei J, Chen Z G and Wu Y 2016 *Sci. Rep.* **6** 32752
- [19] He C, Ni X, Ge H, Sun X C, Chen Y B, Lu M H, Liu X P and Chen Y F 2016 *Nat. Phys.* **12** 1124
- [20] Xia B Z, Liu T T, Huang G L, Dai H Q, Jiao J R, Zang X G, Yu D J, Zheng S J and Liu J 2017 *Phys. Rev. B* **96** 094106
- [21] Zhang Z W, Tian Y, Cheng Y, Liu X J and Christensen J 2017 *Phys. Rev. B* **96** 241306

- [22] Deng Y C, Ge H, Tian Y, Lu M H and Jing Y 2017 *Phys. Rev. B* **96** 184305
- [23] Xie B Y, Liu H, Cheng H, Liu Z Y, Chen S Q and Tian J G 2019 *Phys. Rev. Appl.* **11** 044086
- [24] Xia B Z, Zheng S J, Liu T T, Jiao J R, Chen N, Dai H Q, Yu D J and Liu J 2018 *Phys. Rev. B* **97** 155124
- [25] Lu J Y, Qiu C Y, Deng W Y, Huang X Q, Li F, Zhang F, Chen S Q and Liu Z Y 2018 *Phys. Rev. Lett.* **120** 116802
- [26] Zhang Z W, Tian Y, Wang Y H, Gao S X, Cheng Y, Liu X J and Christensen J 2018 *Adv. Mater.* **30** 1803229
- [27] Tian Z H, Shen C, Li J F, Reit E, Bachman H, Socolar J E S, Cummer S A and Huang T J 2020 *Nat. Commun.* **11** 762
- [28] Deng Y C, Lu M H and Jing Y 2019 *J. Acoust. Soc. Am.* **146** 721
- [29] Nash L M, Kleckner D, Read A, Vitelli V, Turner A M and Irvine W T M 2015 *Proc. Natl. Acad. Sci. USA* **112** 14495
- [30] Wang P, Lu L and Bertoldi K 2015 *Phys. Rev. Lett.* **115** 104302
- [31] Süssstrunk R and Huber S D 2015 *Science* **349** 47
- [32] Mousavi S H, Khanikaev A B and Wang Z 2015 *Nat. Commun.* **6** 8682
- [33] Yu S Y, He C, Wang Z, Liu F K, Sun X C, Li Z, Lu H Z, Lu M H, Liu X P and Chen Y F 2018 *Nat. Commun.* **9** 3072
- [34] Liu Y Z, Lian C S, Li Y, Xu Y and Duan W H 2017 *Phys. Rev. Lett.* **119** 255901
- [35] Tong L, Fan H Y and Xia B Z 2020 *J. Phys. D: Appl. Phys.* **53** 115303
- [36] Huang H B, Tan Z H, Huo S Y, Feng L Y, Chen J J and Han X 2020 *Commun. Phys.* **3** 46
- [37] Li S F, Zhao D G, Niu H, Zhu X F and Zang J F 2018 *Nat. Commun.* **9** 1370
- [38] Kafesaki M and Economou E N 1999 *Phys. Rev. B* **60** 11993
- [39] Chen Y, Xu L, Cai G X and Chen H Y 2018 *Phys. Rev. B* **98** 125430
- [40] Li Y, Wu Y, Chen X and Mei J 2013 *Opt. Express* **21** 7699
- [41] Mei J, Wu Y, Chan C T and Zhang Z Q 2012 *Phys. Rev. B* **86** 035141